AGU100 ADVANCING EARTH AND SPACE SCIENCE

JGR

Journal of Geophysical Research: Oceans

RESEARCH ARTICLE
10.1029/2018JC013763

Special Section:
Sea State and Boundary Layer Physics of the Emerging Arctic Ocean

Key Points:
- In situ data of a large wave event propagating through pancake ice are analyzed for attenuation and directional spreading
- Wave decay through O(10 km)-long transects is predominantly exponential with attenuation rate related to frequency according to a power law
- Observed directional narrowing of the wave spectrum is caused by wave dissipation from pancake ice

Correspondence to:
F. Montiel,
fmontiel@maths.otago.ac.nz

Citation:
Montiel, F., Squire, V. A., Doble, M., Thomson, J., & Wadhams, P. (2018). Attenuation and directional spreading of ocean waves during a storm event in the autumn Beaufort Sea marginal ice zone. *Journal of Geophysical Research: Oceans*, *123*. https://doi.org/10.1029/2018JC013763

Received 7 JAN 2018
Accepted 10 JUL 2018
Accepted article online 23 JUL 2018

Attenuation and Directional Spreading of Ocean Waves During a Storm Event in the Autumn Beaufort Sea Marginal Ice Zone

F. Montiel[1], **V. A. Squire**[1], **M. Doble**[2], **J. Thomson**[3], **and P. Wadhams**[4]

[1]Department of Mathematics and Statistics, University of Otago, Dunedin, New Zealand, [2]Polar Scientific Ltd, Appin, UK, [3]Applied Physics Laboratory, Civil and Environmental Engineering, University of Washington, Seattle, WA, USA, [4]Department of Applied Mathematics and Theoretical Physics, University of Cambridge, Cambridge, UK

Abstract This paper investigates the attenuation and directional spreading of large amplitude waves traveling through pancake ice. Directional spectral density is analyzed from in situ wave buoy data collected during a 3-day storm event in October 2015 in the Beaufort Sea. Two proxy metrics for wave amplitude obtained from energy density spectra, namely, spectral amplitude and significant wave height, are used to track the waves as they propagate along transects through the array of buoys in the predominantly pancake ice field. Two types of wave buoys are used in the analysis and compared, exhibiting significant differences in the wave energy density and directionality estimates. Although exponential decay is observed predominantly, one of the two buoy types indicates a potential positive correlation between wave energy density and the occurrence of linear wave decay, as opposed to exponential decay, in accord with recent observations in the Antarctic marginal ice zone. Factors affecting the validity of this observation are discussed. An empirical power law with exponent 2.2 is also found to hold between the exponential attenuation coefficient and wave frequency. The directional content of the wave spectrum appears to decrease consistently along the wave transects, confirming that wave energy is being dissipated by the pancake ice as opposed to being scattered by ice cakes.

Plain Language Summary Ocean waves in the Arctic Ocean are becoming increasingly energetic as a result of the retreating sea ice caused by climate change. Very little is known of the physical processes governing the interactions between ocean waves in sea ice, however, mainly due to the lack of field data measuring the underlying physics. Here we analyze a data set acquired by a collection of wave measuring devices in the Beaufort Sea over a 3-day period in October 2015, as part of a large experimental program funded by the the U.S. Office of Naval Research. This period coincided with a storm event with waves up to 5 m high. We analyzed the attenuation of such large waves as well as smaller amplitude waves due to the sea ice cover, which mainly consisted of pancake ice. We found that large waves as well as long waves attenuate much more slowly than small waves and short waves. In particular, the more energetic the waves the more likely they are to decay linearly, as opposed to exponentially, with distance, which is in agreement with a similar observation made in the Southern Ocean in 2012. Possible processes causing this effect are discussed in the paper.

1. Introduction

The rapid decline of sea ice extent and volume observed in the Arctic Ocean since 1979 is causing a number of spatial and temporal changes to the morphology of the ice cover. In particular, the Siberian, Chukchi, and Beaufort Seas have experienced significant loss of multiyear sea ice (Comiso, 2012), which is being replaced by less concentrated regions of first year ice, referred to as marginal ice zones (MIZs; Strong & Rigor, 2013). These morphological adjustments are accompanied by a reduced duration of the ice season (Stammerjohn et al., 2012) and a delayed onset of the ice growth season (Thomson et al., 2016). This effective increase of ice-free conditions facilitates the generation of more energetic wind waves and swell, as demonstrated by Thomson and Rogers (2014) using in situ observations in the Beaufort Sea and wave model hindcast simulations. These authors found that the record 2012 summer sea ice minimum opened sufficiently large regions of ice-free waters in the Beaufort Sea, to allow a large storm wave event to develop, reaching a significant wave height (frequency-averaged metric for wave energy density) of 5 m. When such energetic waves impact the MIZ, they may cause the sea ice to fracture into floes and accelerate its melt in summer, further widening the extent of open water regions. This positive wave-ice feedback mechanism was hypothesized by Kohout et al. (2014) when studying the propagation of large storm waves in the Antarctic MIZ. Its impact on sea ice extent in both polar oceans remains unquantified, however, mainly due to the fact that physical processes governing the interactions between ocean waves and sea ice remain poorly understood.

Prompted by the need to forecast wave climate in the increasingly navigable Arctic Ocean (Aksenov et al., 2017; Melia et al., 2016), much recent research has focused on developing and testing parameterizations of sea ice effects on wave propagation in the spectral wave model WAVEWATCH III® (hereinafter referred to as WW3). This numerical model describes the transport of the directional wave spectrum over the world's oceans. It contains a number of so-called source terms that parametrize the effects of physical processes on wave transport. Of relevance to the present study is the source term quantifying (i) the attenuation of wave energy in ice-covered oceans and (ii) the changes in wave directionality, usually referred to as directional spreading. Physical mechanisms responsible for these effects can be broadly classified into conservative scattering and dissipative processes. Scattering of waves by inhomogeneities in the MIZ, for example, ice floe or thickness variations, does not dissipate wave energy but redistributes it into adjacent directional components of the spectrum. Dissipative processes, such as turbulence, ice creep, wave overwash and wave-induced collisions or breakup of floes, remove energy from the wave spectrum. The relative importance of each of these processes on wave propagation in ice-covered seas largely depends on the morphology of the sea ice.

In the latest version of WW3, six options for the sea ice source term are available (The WAVEWATCH III® Development Group, 2016). They are either parameterizations of the outputs of separate models or empirical. Although the former class of parameterizations is still in its infancy, mainly due to its inability to resolve the dissipative physics of the wave/ice system in an inhomogeneous ice cover (Mosig et al., 2015), scattering effects depending on ice morphology are now included with a representation of directional spreading and ice floe breakup, noting that the most recent modeling advances in this area (e.g., Montiel & Squire, 2017; Montiel et al., 2016) are yet to be integrated. Empirical parameterizations describe the spatial attenuation rate of waves due to sea ice as functions of frequency (based on data reported by Meylan et al., 2014; Wadhams et al., 1988) or significant wave height (based on Kohout et al., 2014). These parameterizations, as well as a few other data sets not parametrized in WW3, are fundamental to all future developments of the software as they constitute benchmark results against which new models should be tested.

In response to the need to represent ocean/ice/atmosphere interactions in large-scale forecasting models more faithfully, in 2013 the U.S. Office of Naval Research initiated the 5-year Departmental Research Initiative Sea State and Boundary Layer Physics of the Emerging Arctic Ocean (hereafter referred to as the Sea State DRI), with a focus on gaining a better understanding of the physical processes governing the start of the ice growth season as a way to inform future model developments (Thomson et al., 2017, 2018). In order to achieve this, a 6-week voyage took place in October and November 2015 in the Chukchi and Beaufort Seas, where pancake ice, which forms in the presence of waves, was the dominant ice type encountered during the experiment. A detailed account of the measurements conducted during the Sea State voyage, as it will be referred to subsequently, has been reported by Thomson (2015).

Seven wave experiments (WEs) were conducted during the Sea State voyage. In each experiment, an array of drifting wave sensors was deployed for a period ranging from a few hours to a few days and recorded pointwise directional wave spectra. Three types of wave sensors were used during these experiments: SWIFT (Thomson, 2012), WB (Doble et al., 2015), and NIWA buoys, the latter being a variant from the WIIOS (Kohout et al., 2015). A total of 18 individual wave sensors (eight SWIFTs, nine WBs, and one NIWA) was used as part of the voyage. The SWIFT and WB buoys, which are devices floating in open water, were cross-calibrated prior to reaching the ice edge and can be used in low ice concentration zones. In contrast, the NIWA buoy must sit on top of an ice floe with size larger than 10 m, making it more suitable to measure waves deeper into the ice-covered oceans. Each WE was conducted for a specific purpose, for example, measuring wave reflection/transmission by an ice edge band or wave scattering by a small compact array of medium size floes.

In this paper, we analyze the directional wave data from a WE designed to measure the attenuation of a large wave event, with significant wave height reaching at least 4 m, traveling through a large field of pancake ice. Dissipative processes are expected to dominate over scattering for this type of ice cover (Doble et al., 2015; Rogers et al., 2016). In situ quantitative observations of large wave events in ice-covered seas have been reported in the Antarctic MIZ (Doble et al., 2015; Kohout et al., 2014; Meylan et al., 2014) but, to our knowledge, not in the Arctic Ocean. Key findings from the analyses of the Antarctic data sets are (i) the significant wave height decays exponentially for low-energy waves and linearly for high-energy waves (Kohout et al., 2014) and (ii) frequency-resolved components of wave amplitude decay exponentially with their attenuation coefficient proportional to a power of wave frequency and independent of the magnitude of wave energy density (Doble et al., 2015; Meylan et al., 2014). The latter finding mirrors what was found in the Arctic Ocean during earlier wave attenuation experiments (e.g., Wadhams, 1975; Wadhams et al., 1988) and suggests that using the linear theory of water waves is a valid approach for wave/ice interactions. The observation of linear decay of significant wave height for large waves has puzzled the wave/ice research community, however, as no model has been able to replicate this behavior and no physical process has been suggested to explain it. Since linear decay does not approach 0 asymptotically, such a phenomenon can only be envisaged in a restricted spatial region or as part of a short-lived unstable regime.

Our main goal here is to determine the type of wave decay observed for the data set analyzed and its relationship to wave frequency and energy density. Both frequency-averaged and frequency-resolving standard metrics of wave amplitude, derived from the energy spectral density, are considered, which will be defined in sections 3.1 and 4. We propose to fit a decay model accommodating both linear and exponential decay as extreme cases through wave amplitude proxy profiles extracted from the data. An optimization routine then determines which type of decay best fits the data and estimates the goodness of fit. We also seek to quantify how wave directionality changes with distance into the pancake ice cover, as such observations do not exist for this type of ice cover (Sutherland et al., 2018; Sutherland & Gascard, 2016; Wadhams et al., 1986, discuss the only other three data sets we are aware of but for an MIZ dominated by ice floes).

2. Wave Observations

During the Sea State voyage, a WE was initiated on 10 October 2015 after the ship reached the ice edge in the Western Beaufort Sea at approximate latitude 73° N. Four SWIFTs, two WBs, and the NIWA buoy were deployed as pancake ice was forming intensively in a 1-m swell. After receiving reports of decreasing fetch for these waves, most of the buoys were recovered and the WE was shifted south at approximate latitude 72.5° N, where a large wave event was forecasted to generate 4-m waves. The NIWA and two SWIFT buoys remained in the original location to measure waves deeper into the ice. We do not consider the data collected by these buoys in the subsequent analysis.

The wave event took place on 11–14 October and was the result of strong winds reaching 23 m/s at 10 m above sea surface in the central and eastern parts of the Beaufort Sea. The presence of a low and high counterrotating pressure system, south and north of this region, respectively, is believed to have been responsible for the observed atmospheric conditions. Rogers et al. (2016) provide additional quantitative details on the generation of this wave event.

On 11 October, an array of six SWIFT and five WB wave sensors spanning approximately 60 km of ice-covered ocean was deployed as pancake ice was rapidly forming. Direct ship-based observations suggest that ice concentration along the transect of buoys ranged from 50% to 100%, while thickness was less than 25 cm (Rogers et al., 2016). As the storm developed, significant wave height (defined later) increased from 1 to 3 m in the region of study over a period of a few hours. Winds at 10 m above sea surface reached 16 m/s and significant wave height peaked at 4–5 m in the early morning of 12 October. The buoys were recovered on 13 and 14 October, as the wave event eased to significant wave heights of 2–3 m.

Figure 1a depicts that the trajectory of all the buoys deployed during the WE started on 11 October. The labels associated with the buoys in the figure are those assigned to each physical buoy for the duration of the voyage. The buoys deployed further north on 10 October are not shown in this figure for clarity. Time series of the significant wave height (H_s), frequency-averaged mean wave direction (θ_0), and frequency-averaged directional spreading (σ_0) for each buoy are shown in Figures 1b–1d, respectively. Although these quantities will be defined rigorously in section 4, we can interpret H_s as a measure of the wave energy, θ_0 as the dominant direction of wave propagation (measured positively counterclockwise, with $\theta_0 = 0$ pointing to the east) and σ_0 as the spread of wave directions around θ_0.

All the buoys appear to have drifted northwest during the storm event (see panel a in Figure 1), which accords with the mean wave direction of 100–120° consistently observed in panel c. Qualitatively, the significant

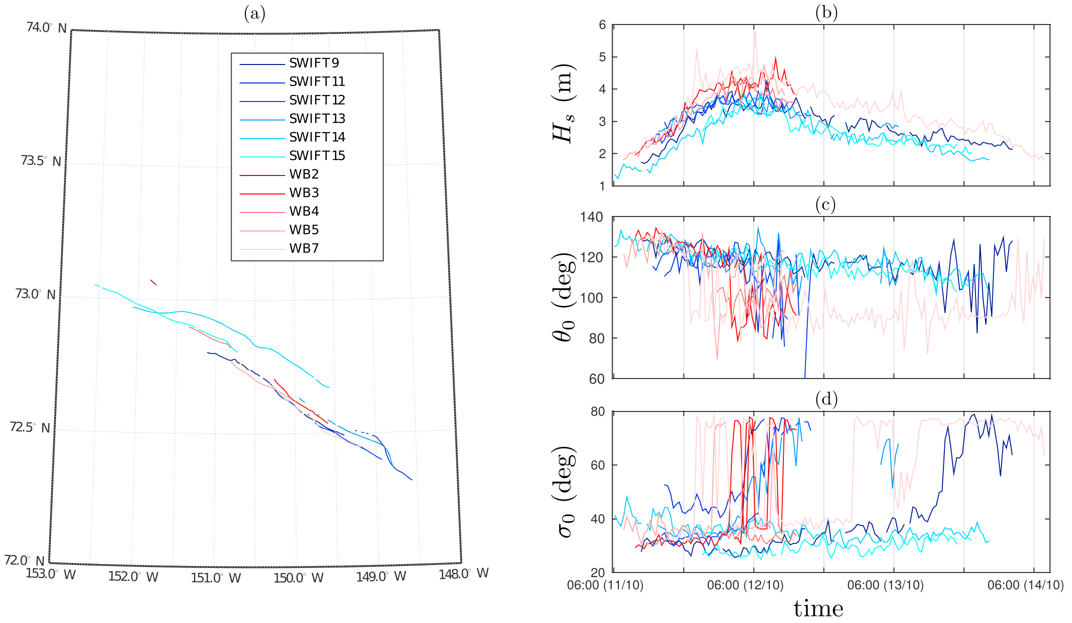

Figure 1. (a) Trajectories of the six SWIFT and five WB buoys (blue and red shaded, respectively) deployed on 11 October. On the right-hand side panels, time series of (b) the significant wave height H_s, (c) the frequency-averaged mean wave direction θ_0, and (d) the frequency-averaged directional spread σ_0 are depicted for each of these 11 buoys. The color code used in these panels to distinguish buoys is the same as that of panel a.

wave height evolves in a similar way for all the buoys over the duration of the WE, with a buildup of the wave event from 11 October at 06:00 UTC, peaking at around 06:00 UTC on 12 October and decreasing over the following 2 days. The observed quantitative differences of significant wave height between the different buoys are expected. The presence of sea ice on the surface of the ocean attenuates wave energy with distance from the ice edge, so buoys located farther north should measure less wave energy. There is a difference between H_s measured by SWIFT (blue lines) and WB (red lines) buoys, however, which cannot be explained by the latitudinal position of the buoys. More specifically, the significant wave height measured by SWIFT buoys is consistently less than that retrieved from WB buoy measurements. This discrepancy is exacerbated after 18:00 UTC on 11 October, which correlates with mean direction and directional spreading starting to behave erratically, particularly for the WB buoys.

Synthetic aperture radar imagery revealed that a significant ice retreat took place during the night of 11 and 12 October (Rogers et al., 2016), that is, at the peak of the wave event. As a result, some wave buoys were likely to be in open water during part of the wave event, where directional measurements are less precise due to the broader wave spectrum. Although the ice retreat may have contributed to the differences between SWIFT and WB buoy wave measurements, it remains unclear why WB buoys appear to measure more energetic swell than the SWIFT buoys. During their recovery, it was observed that both buoy types experienced significant icing, which will have affected the hydrodynamical properties of the two buoy types differently, given that their geometries differ significantly. More specifically, some SWIFT buoys were observed to have capsized and were laying horizontally in an almost neutrally buoyant state, which may have affected their ability to follow the ocean surface appropriately. In contrast, WB buoys were designed to have more reserve buoyancy, so that icing is less likely to have affected the measurements of heave. Icing caused dropouts in heading for the WB systems, which derived their heading from a dual-GPS compass (Hemisphere H-102) rather than the more usual magnetometers, in a bid to overcome issues with proximity to the magnetic pole. Also, heading was recorded only at minute intervals (versus 50 Hz for the wave data) as the observed significant rotation of the WB buoys down the face of large waves was unexpected. This heading was subsequently upsampled (cubic spline) to match the wave data sampling interval before the recorded buoy-referenced directions were rotated into Earth coordinates, which may introduce errors. It has also been suggested that the SWIFT's high-pass filter used in the experiment, which is designed to remove periods longer than 25 s, was too severe, causing wave energy density at all frequencies to be a little low compared to those computed from the WB data sets.

The subsequent analysis of wave attenuation and directional spreading during the wave event is conducted for the two buoy types separately.

3. Data

We analyze the processed wave data collected by each SWIFT and WB wave sensor, which are available on the Google Drive repository created by the science team of the Sea State DRI (see Acknowledgments section for additional details). For each wave buoy, we extract (i) the wave energy spectral density $E(t,f)$ and (ii) the normalized spectral moments $a_1(t,f)$, $b_1(t,f)$, $a_2(t,f)$, and $b_2(t,f)$, which can be used to approximate the directional spectrum at a buoy location as

$$S(t,f,\theta) \approx E(t,f)\left\{\frac{1}{2} + \sum_{n=1}^{2}\big(a_n(t,f)\cos n\theta + b_n(t,f)\sin n\theta\big)\right\} \tag{1}$$

for each time t, frequency f, and direction θ.

The processed spectral density E and the normalized spectral moments a_n and b_n, $n = 1,2$, are provided as averages over 30-min time intervals. The time intervals are centered at 15 and 45 min past the top of each hour for the SWIFT buoy data, while they are centered at 0 and 30 min past the top of each hour for the WB buoys. As a consequence, we have shifted all WB time intervals 15 min forward in time to create a consistent timeline for both data sets. This time shift has no impact on the subsequent analysis as the SWIFT and WB buoy data sets are analyzed separately, as discussed in section 2.

The discrete frequency components also differ for the two buoy types, as they are given by $f_j^S = 0.0098 + (j-1)\Delta f^S$ Hz, $j = 1,\ldots,42$, for the SWIFT buoys, and $f_j^W = 0.0557 + (j-1)\Delta f^W$ Hz, $j = 1,\ldots,46$, for the WB buoys, where the frequency increments are $\Delta f^S \approx 0.0117$ Hz and $\Delta f^W \approx 0.0097$ Hz, respectively. For consistency between the two buoy types, we linearly interpolated the spectral density and normalized spectral moments provided for the WB buoys onto the frequency components of the SWIFT buoys.

3.1. Wave Energy Density

Wave energy spectral density measurements are used to describe the attenuation experienced by the waves as they travel through the ice-covered ocean. Recent analyses of in situ wave observations in the Antarctic MIZ (composed of ice floes as opposed to pancake ice) showed that the way in which waves attenuate through the MIZ depends on which wave amplitude metric is considered in the analysis. Specifically, Meylan et al. (2014) found that the spectral amplitude, which is proportional to $\sqrt{E(t,f)\Delta f}$ and is therefore frequency resolving, consistently attenuates exponentially for each frequency component, with the rate of attenuation depending on frequency. On the other hand, Kohout et al. (2014) found that the significant wave height, which is a frequency-averaged quantity, attenuates linearly for large-amplitude waves and exponentially for small-amplitude waves. The physical processes governing the observed linear decay of energetic waves are not understood, although they must be of a nonlinear nature since linear physics invariably predicts exponential decay. Note that amplitude/height metrics were used as proxies for energy density in both studies. Here we investigate wave decay using both the spectral amplitude, defined later in equation (8), and the significant wave height defined as

$$H_s(t) \approx 4\left(\int_{f_1^S}^{f_{42}^S} E(t,f)\,\mathrm{d}f\right)^{1/2}, \tag{2}$$

at the center t of each time interval (see section 2 and Figure 1b for a discussion on the significant wave height data).

Figure 2 shows the spectral density E plotted against frequency for all the buoys active at 17:15 UTC on 11 October (see left panel), that is, as the large wave event was still developing ($H_s < 3$ m), and at 05:45 UTC on 12 October (see right panel), that is, at the peak of the wave event ($H_s > 3$ m). A 5-point moving average procedure was applied to smooth the energy spectra. In calm sea conditions (17:15 UTC on 11 October), the peak frequency of the spectra is $f_p \approx 0.115$ Hz corresponding to a peak period of $T_p \approx 8.7$ s. The southernmost SWIFT buoys, that is, SWIFT11, SWIFT13, and SWIFT12, reach $E \approx 6\,\mathrm{m}^2 \cdot \mathrm{s}$ at the peak frequency, dropping down to $E < 5\,\mathrm{m}^2 \cdot \mathrm{s}$ for the two northernmost ones, suggesting some attenuation due to the presence of sea

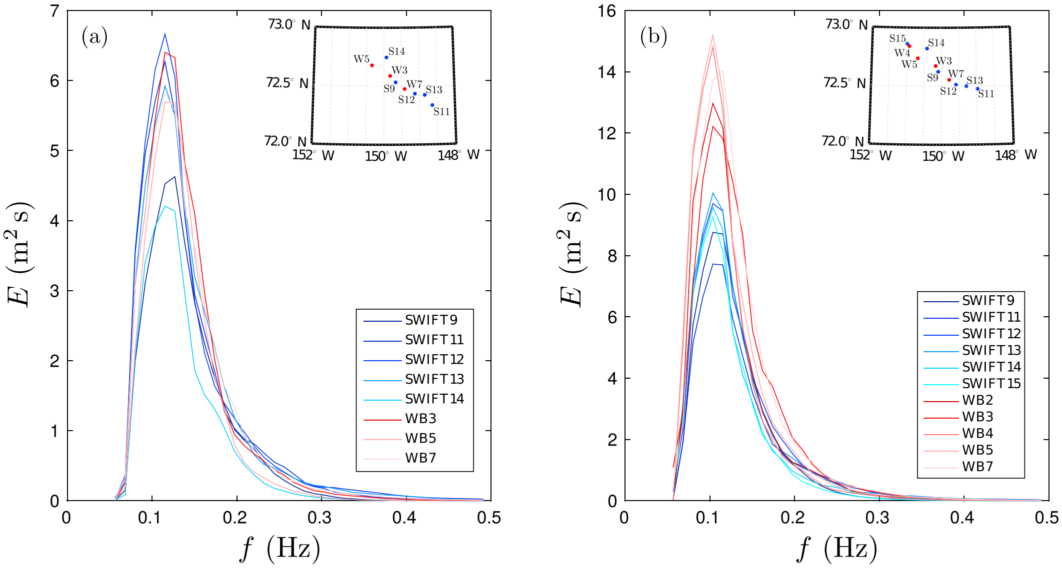

Figure 2. Wave energy spectral density E plotted against frequency f for all the buoys active during the time intervals centered at (a) 17:15 UTC on 11 October and (b) 05:45 UTC on 12 October. The location of the buoys at these time intervals is shown in the insets. The same colors as in Figure 1 are used here.

ice. Closer inspection of the SWIFT buoy spectra shows that there is some level of attenuation over the entire frequency range. On the other hand, spectral densities of the three WB buoys around the peak frequency have similar magnitudes to the three southernmost SWIFT buoys, despite the fact that they are in the vicinity of the northernmost SWIFT buoys. This suggests that the discrepancy reported in section 2 between SWIFT and WB significant wave heights is most pronounced around the peak frequency. We further observe that no attenuation in spectral density can be seen for the WB buoys around the peak frequency, as the northernmost and southernmost buoys (WB5 and WB7, respectively) have similar spectra in this frequency range, while WB3 measures the most energetic waves.

Our observations of differences between SWIFT and WB buoy wave energy spectral densities are further reinforced upon inspection of the rough sea condition spectra in Figure 2b. The peak frequency has now shifted down to $f_p \approx 0.103$ Hz corresponding to a peak period of $T_p \approx 9.7$ s. Spectral densities around the peak frequency are clearly different for the SWIFT and WB buoys, with $E < 10\,\mathrm{m}^2 \cdot \mathrm{s}$ at the peak for the former buoy type and $E > 12\,\mathrm{m}^2 \cdot \mathrm{s}$ for the latter. It is therefore clear that WB buoys are measuring larger wave energy than SWIFT buoys, particularly around the peak frequency, which probably arises from the effect of icing on the SWIFT buoys heave response. As opposed to the calm sea spectra, no clear attenuation of energy around the peak frequency can be observed here for the SWIFT spectral densities. In particular, the two northernmost buoys, that is, SWIFT14 and SWIFT15, are not associated with the lowest measured energy levels around the peak frequency. As discussed earlier, the ice retreat observed during the peak of the wave event may be a cause of the apparent absence of wave attenuation, although we note that for $f > 0.13$ Hz, spectral densities seem to show attenuation. The method discussed in section 4 is intended to quantify the type and rate of wave attenuation.

3.2. Wave Directionality

We also seek to quantify how the directionality of the wavefield changes as waves propagate in the pancake ice cover, as this may inform what the dominant processes governing wave-ice interactions are in this particular experiment. There is observational (see ; Sutherland & Gascard, 2016; Wadhams et al., 1986) and theoretical (see Montiel et al., 2016; Squire & Montiel, 2016) evidence suggesting that short waves traveling through the MIZ tend to experience a broadening of the range of wave directions as a result of wave scattering by the constituent ice floes, while long waves have been hypothesized to experience a decrease in their directional range, likely caused by dissipative effects gradually filtering out spectral components. Since dissipative effects dominate over scattering in pancake ice, we expect this latter scenario to govern our wave directionality data. We note that, to the best of our knowledge, no observational evidence of directional narrowing in pancake ice exists.

The directionality of the wave spectrum is quantified by the mean wave direction $\theta_1(t,f)$, which characterizes the dominant wave direction, and the directional spread $\sigma_1(t,f)$, which measures the spread of angular components around θ_1. They are expressed in terms of the normalized spectral moments a_1 and b_1 introduced earlier, as (Kuik et al., 1988; Wadhams et al., 1986)

$$\theta_1(t,f) = \tan^{-1}\left(b_1(t,f)/a_1(t,f)\right) \tag{3}$$

and

$$\sigma_1(t,f) = \sqrt{2}\left(1 - \sqrt{\left(a_1(t,f)\right)^2 + \left(b_1(t,f)\right)^2}\right)^{1/2}. \tag{4}$$

Both θ_1 and σ_1 are angles that are expressed in radians, which we convert to degrees to carry out the analysis.

Figure 3 shows the mean wave direction (top panels) and directional spread (bottom panels) for each buoy at the two time intervals considered in Figure 2, that is, during the developing storm (left panels) and at the peak of the storm (right panels). The same smoothing procedure was applied to the directional data as for the spectral density. In the prestorm time interval, the mean wave direction is remarkably consistent between all the buoys (both SWIFT and WB) around the peak frequency (see panel a), suggesting that the ice cover is sufficiently homogeneous not to cause wave refraction. The variability of the mean wave directions measured by the buoys also seems to increase with frequency, as these wave components are more susceptible to the effects of ice-induced dissipation. At the peak time of the wave event (see panel b), much variability is observed over the entire frequency range, most likely as a consequence of the observed icing on the buoys causing less reliable directional information.

In prestorm conditions, the frequency dependence of the directional spread is similar for almost all buoys in the low- to middle-frequency range, while there is more variability at high frequency (see panel c). The directional spread reaches a minimum value of $\sigma_1 = 20–25°$ at the peak frequency and increases to values larger than 60° at lower and higher frequencies. Only the directional spread measured by SWIFT11 is different, particularly around the peak frequency, where the minimum reached is close to 40°. Referring to the inset of Figure 2a, SWIFT11 is the southernmost wave buoy at that time interval, so the higher values of the directional spread suggest that directional spreading decreases with distance of propagation in the pancake ice cover, most likely as a result of directional filtering from dissipative processes. The abrupt change of directional spread between SWIFT11 and all the other buoys around the peak frequency is likely explained by the lack of sea ice at the location of this buoy, as observed during deployment. At higher frequencies, σ_1 values for SWIFT11 remain higher than those of other SWIFT buoys, even though the variability between buoys is higher. In contrast, directional spread of the three WB buoys increases to values larger than that of SWIFT11 at high frequency even though the three buoys are at higher latitudes. Similar observations can be made at the peak storm interval (see panel d), in which the directional spread of SWIFT buoys decreases consistently with increasing latitude of the buoy. At buoys SWIFT11 and SWIFT13, σ_1 is much higher than at the other buoys, suggesting these two buoys are in locations with lower concentration or in open water. In particular, SWIFT11 takes values of $\sigma_1 \approx 70°$ at the peak frequency, which can be interpreted as a confused sea without a well-defined single direction of swell propagation, noting that the theoretical directional spread value of isotropy is approximately 81°.

For the purpose of later discussions, we introduce a frequency-averaged version of the mean wave direction and the directional spread, which we define as

$$\theta_0(t) = \frac{16}{H_s(t)^2}\int_{f_1^S}^{f_{42}^S} \theta_1(t,f)E(t,f)\,\mathrm{d}f \quad \text{and} \quad \sigma_0(t) = \frac{16}{H_s(t)^2}\int_{f_1^S}^{f_{42}^S} \sigma_1(t,f)E(t,f)\,\mathrm{d}f, \tag{5}$$

respectively. The physical relevance of these averaged quantities is only valid for a unimodal directional wave spectrum (i.e., swell only or wind wave only). Inspection of the spectra does not show the existence of a wind wave peak. The energy density weighting factor used in these expressions further filters out high frequency components, so that the frequency-averaged directional mean wave direction and the directional spread principally measure directionality of the swell regime. We have discussed these quantities in section 2.

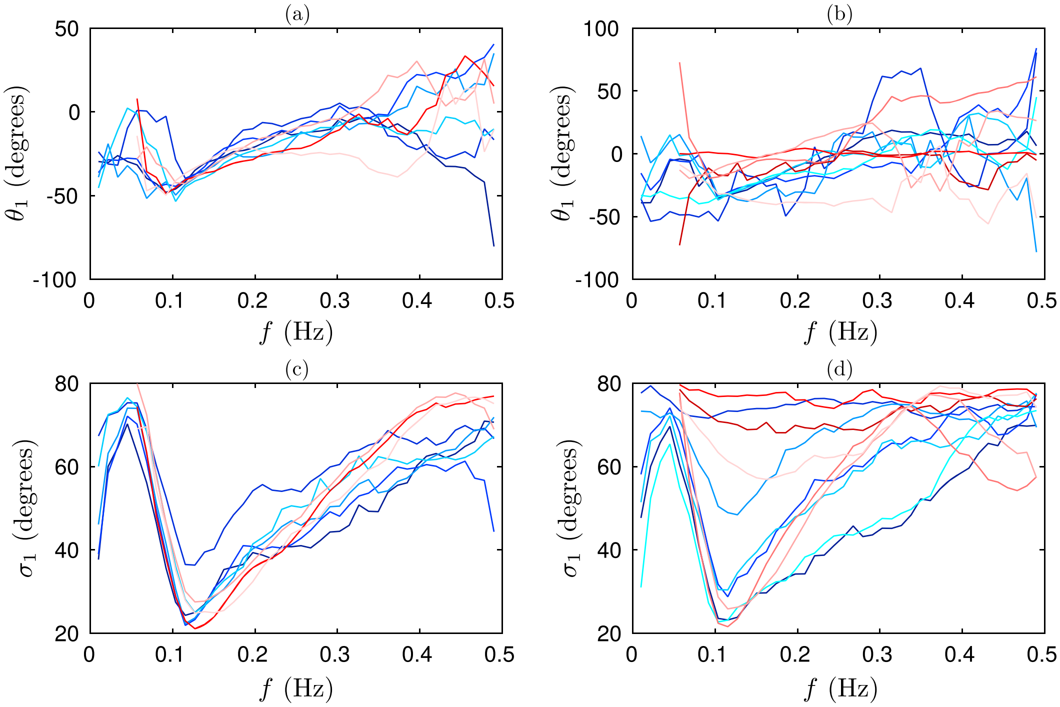

Figure 3. Mean wave direction θ_1 (top panels a and b) and directional spread σ_1 (bottom panels c and d) plotted against wave frequency. The left panels a and c show θ_1 and σ_1, respectively, for all active buoys during the time interval centered at 17:15 UTC on 11 October, that is, in calm wave conditions. The right panels b and d show these quantities for the time interval centered at 05:45 UTC on 12 October, that is, in storm wave conditions. Colors are the same as in Figure 3.

4. Methods

Most past observational studies investigating wave energy attenuation in the MIZ (for both pancake ice and ice floes) are based a priori on the key assumption that wave energy decays exponentially with distance from the ice edge. Based on this assumption, the rate of exponential attenuation is typically estimated by fitting an exponential decay curve to pairs of buoy energy density or amplitude measurements, either frequency-resolving or frequency-averaged (see, e.g., Cheng et al., 2017; Kohout et al., 2014; Meylan et al., 2014). Although this approach maximizes the number of attenuation rate estimates for a data set, it prevents assessment of goodness of fit and typically rejects any wave growth cases that can occur for a random sea state. Here we describe a method to estimate wave energy attenuation and directional spreading based on measurements at three buoys or more, thereby allowing us to quantify the performance of the data fitting procedure on a potentially fluctuating decay profile, as well as allowing for the possibility of nonexponential decay profiles.

We first introduce wave transects along which energy attenuation and directional spreading are estimated. Each transect is a straight line on the planar ocean, that is, neglecting Earth's surface curvature, which is defined by a point and a direction. The point is identified with the location of the southernmost active buoy at each time interval. The direction of each transect is defined as the weighted sample mean of the mean wave direction measured at the $N_b \geq 3$ active buoys during that time interval, that is,

$$\bar{\theta}(t,f) = \sum_{p=1}^{N_b(t)} w_p(t,f)\theta_1^{(p)}(t,f), \tag{6}$$

where for each buoy $p = 1, \ldots N_b$, $\theta_1^{(p)}(t,f)$ is the mean wave direction given by (3) and $w_p(t,f)$ is a normalized weighting factor. We have introduced the superscript p in the mean wave direction to emphasize each buoy's dependence on these functions, which was implied until now. It should further be noted that N_b is the total number of buoys of a particular type, that is, either SWIFTs or WBs, so that the transects for the two buoy types are potentially different. The weighting factors in (6) are defined by

$$\frac{1}{w_p(t,f)} = \sigma_1^{(p)}(t,f)^2 \sum_{q=1}^{N_b(t)} \frac{1}{\sigma_1^{(q)}(t,f)^2}, \tag{7}$$

where $\sigma_1^{(p)}(t,f)$ is the directional spread estimated at buoy p from (4). Here the directional spread is interpreted as the standard deviation of the probability distribution described by the directional spectrum $S(t,f,\theta)/E(t,f)$, so that the direction of the transect $\bar{\theta}(t,f)$ is the maximum likelihood estimator of the mean of the probability distribution. Therefore, wave buoys measuring a larger directional spread contribute a lower weighting factor to the transect direction estimate.

At each time interval t and frequency f, we create a wave amplitude (defined below) profile along the corresponding transect, where each wave buoy amplitude estimate is projected perpendicularly from the buoy location onto the line transect. The underlying assumption is that each frequency component of the wavefield is a long-crested wave traveling in the direction of the transect. Wind speed and directions at 10 m during the wave event discussed here were analyzed by Rogers et al. (2016) using the Navy Global Environmental Model. Their results seem to indicate that the strong winds in the Beaufort Sea during the wave event were reasonably homogeneous, suggesting that the wavefield incident on the array of buoys follows the same pattern. Spatial inhomogeneities can be quite significant on short time scales, however, which may be a source of noise in the data when analyzed in a transect.

Here by amplitude we mean the spectral amplitude $A(t,f)$, corresponding to the energy density contribution of a bin of frequency of width Δf^S and centered at frequency f to the total energy density in each time interval centered at t, that is (see ; Meylan et al., 2014),

$$A(t,f) = \sqrt{2E(t,f)\Delta f^S}. \tag{8}$$

Wave attenuation along each profile is estimated by fitting a decay curve defined by the ordinary differential system

$$\frac{\mathrm{d}A}{\mathrm{d}s} = -\alpha A^n, \quad \text{with} \quad A(0) = A_0, \tag{9}$$

where $\alpha > 0$, n, and A_0 are parameters of the curve to be optimized as part of the fitting procedure. Here s is the linear coordinate measuring distances along the transect, such that $s = 0$ at the location of the southernmost buoy and $s > 0$ in the direction of $\bar{\theta}$.

Equation (9) originates from Shen and Squire (1998), who consider how wave amplitude is dissipated by a granular medium composed of colliding pancakes of sea ice that are much smaller in diameter than the wavelength. This equation also describes wave attenuation through a homogeneous viscous layer governed by a power law (i.e., non-Newtonian) fluid constitutive relation, in which the viscosity is proportional to the effective strain rate raised to the power $(1-n)/n$. When $n \in (0,1)$, viscosity increases with increasing strain rate, in which case the material is referred to as dilatant. When $n \notin (0,1)$, the viscosity decreases as strain rate increases and the material is described as pseudoplastic. Because shorter period waves attenuate more rapidly than longer ones in sea ice, that is, the effective viscosity of the wave/sea ice system increases as frequency and therefore strain rate increases, the phenomenon of wave-ice interaction, as opposed to sea ice itself, is dilatant. In the subsequent analysis, we restrict the parameter n to take values in the interval $(0,1)$, in order to enforce this relationship between attenuation rate and frequency. The limiting cases $n \to 0$ and $n \to 1$ are particularly important as they approach the extreme behaviors of linear and exponential decay, respectively. We noted earlier that these two types of decay were observed for the same Antarctic data set by looking at different standard wave amplitude/height metrics (Kohout et al., 2014; Meylan et al., 2014). Here our goal is to assess the tendency of each wave amplitude attenuation profile to be either linear or exponential and determine if the same differences in decaying profiles emerge as for the Antarctic MIZ data set.

To implement the fitting procedure, we express the spectral wave amplitude A as a function of the transect coordinate s. Solving (9), we obtain

$$A(s) = \left(A_0^{1-n} - (1-n)\alpha s\right)^{\frac{1}{1-n}}. \tag{10}$$

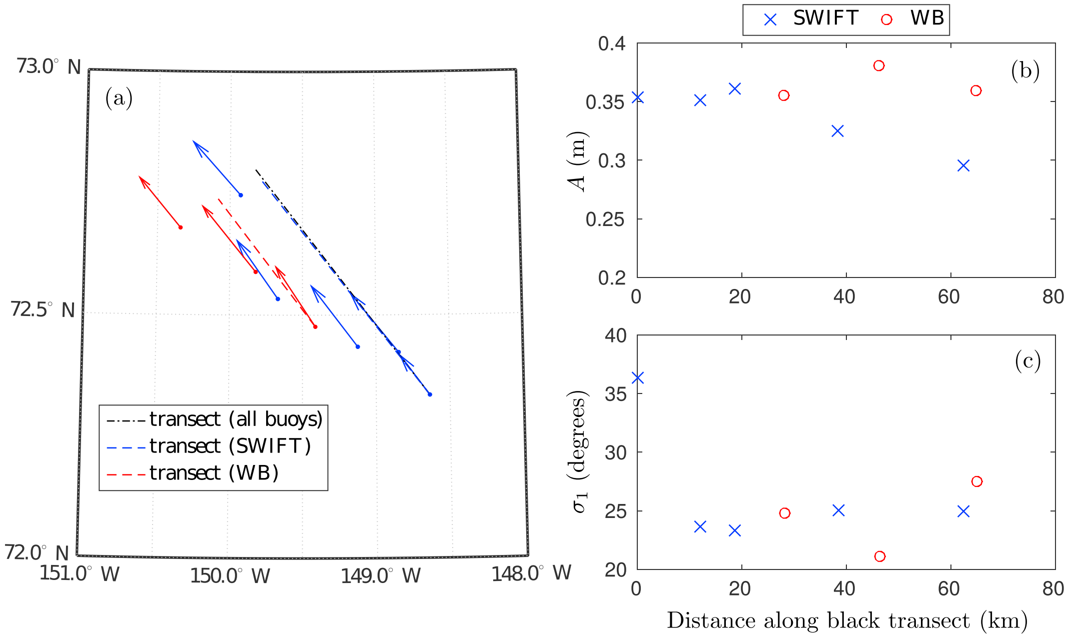

Figure 4. (a) Wave directionality of the active buoys at the prestorm time interval considered in Figure 2a and at frequency $f = 0.125$ Hz. Each arrow points in the mean wave direction $\theta_1^{(p)}(t,f)$ of a buoy p and has magnitude inversely proportional to the directional spread $\sigma_1^{(p)}(t,f)$. Transects defined in (6) for the SWIFT and WB buoys are shown as blue and red dashed lines, respectively. The transect obtained from wave directionality data of all SWIFT and WB buoys combined is also depicted as a black dash-dotted line and is used to plot (b) the spectral wave amplitude A and (c) the directional spread σ_1 profiles for all the buoys along this transect.

We use the built-in Matlab nonlinear least square solver *lsqnonlin* to estimate the parameters α, n, and A_0 that best fit the wave energy data along each transect. This routine implements the trust region reflective algorithm, which can handle bounds on the estimated parameter, but requires at least as many data points as parameters to estimates, that is, $N_b \geq 3$ as specified earlier. In some cases, the algorithm returns complex parameter values, typically when the spectral amplitude data are small so that the term within the large brackets of (10) is negative. When this occurs, we discard the estimated parameters. The goodness of fit of the model to the data is estimated via the coefficient of determination R^2, which we compute for each amplitude attenuation profile.

To estimate the rate of directional spreading along each transect, we conduct a similar curve fitting procedure as for spectral amplitude profiles. We only seek to determine whether the directionality of the wavefield broadens or narrows with distance from the ice edge at each time interval t and frequency f, however. Therefore, we fit a simple linear curve through the directional spread measurements $\sigma_1(t,f)$ projected on the transect (in the same way as we did with the wave energy data), giving

$$\sigma_1(s) = \beta s + C, \tag{11}$$

where β and C are the curve fitting parameters, which are estimated using linear least squares.

Figures 4a and 5a show the transects determined with our method at the prestorm and peak storm time intervals considered earlier, respectively, and at frequency $f = 0.125$ Hz. The operational SWIFT and WB buoys are shown as blue and red dots, respectively. Each arrow points in the mean wave direction θ_1 measured by the corresponding buoy and its magnitude is proportional to the inverse of the directional spread σ_1. We observe that in the prestorm time interval (see Figure 4), all the arrows (for both SWIFT and WB buoys) are long and are pointing in approximately the same direction, indicating a narrowly spread swell is traveling in the ice-covered ocean with little directional change. This is consistent with the minimum in directional spread seen in Figure 3c at $f \approx 0.125$ Hz. On the other hand, at the peak of the storm event (see Figure 5), the directionality of the wavefield between the two buoy types is incompatible, so that the SWIFT and WB transects are significantly different.

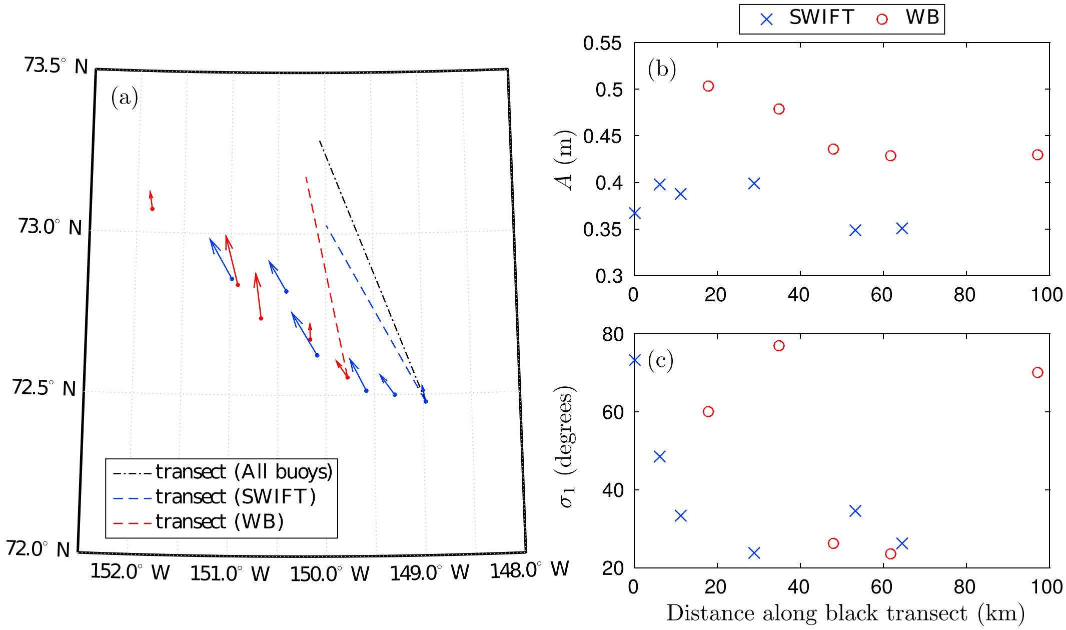

Figure 5. Same as Figure 4 for the peak storm time interval considered in Figure 2b.

To compare the wave spectral amplitude and directional spread data of the two buoy types, we define a third transect with direction determined by (6) in which the contribution from both the SWIFT and WB buoys is taken to compute the weighted mean. These transects are shown in black in Figures 4a and 5a. The upper and lower right panels of these figures depict the spectral amplitude and directional spread profile along the black transect, respectively. In Figure 4 (i.e., in prestorm conditions), the spectral amplitude and directionality data of the two buoy types are reasonably concordant, although we note WB amplitude data are larger than SWIFT amplitude data ($<$ 0.33 m for SWIFTs versus $>$ 0.35 m for WBs) farther than 30 km along the transect and do not seem to experience attenuation. In Figure 5 (i.e., in peak storm conditions), the discrepancy between the SWIFT and WB data is apparent for both spectral amplitude and directional spread, as WB amplitude data are consistently larger than SWIFT data by a margin of approximately 0.1 m, and the WB directional spread data behave more erratically than the SWIFT ones, varying between ~20° and 80°, that is, near isotropy, which may again be due to unreliable WB directional data caused by icing.

We now show examples of the curve fitting procedure on the data depicted in Figures 4 and 5. The spectral amplitude and directional spread data are shown in panels a–d and e–h, respectively, of Figure 6, for SWIFT (blue) and WB (red) buoys separately and along their particular transects. The fitted curves, that is, (10) for spectral amplitude profiles and (11) for directional spread profiles, are also displayed on each panel. At the prestorm time interval (four leftmost panels), the curve fitting procedure predicts a near-linear decay through the SWIFT spectral amplitude data (see panel a) with fit parameters $A_0 \approx 0.3644$, $\alpha \approx 1.025 \times 10^{-6}$, and $n \approx 1.840 \times 10^{-6}$ (units have been omitted deliberately) and a coefficient of determination $R^2 \approx 0.86$, confirming the good fit observed visually. The procedure does not work for WB spectral amplitude data (see panel b), however, as it seems to exhibit unrealistic wave growth. At the peak storm interval (four rightmost panels), we obtain a near-linear decay (with $n \approx 0.0214$) for the SWIFT data (see panel c) and a near-exponential decay (with $n \approx 0.9999$) for the WB data (see panel d). Note the low value of $R^2 = 0.42$ in panel c, which is probably explained by the significant variability of spectral amplitude data in the first 30 km of the transect. The directional spread data fitting clearly shows a narrowing directional spread for the SWIFT data at both time intervals (see panels e and g) and a broadening directional spread for the WB data at the prestorm interval (see panel f). The large variability of the WB spread data at the peak storm interval (see panel h) does not allow us to find a trend.

The case studies considered in this section have further highlighted the discrepancies between the two buoys in terms of both wave energy density and directional data. This suggests that design and sensor differences may have supplementary effects in the harsh polar marine environment in which the experiment took place, despite the devices having been previously cross-calibrated in open water. Because of the unreliability

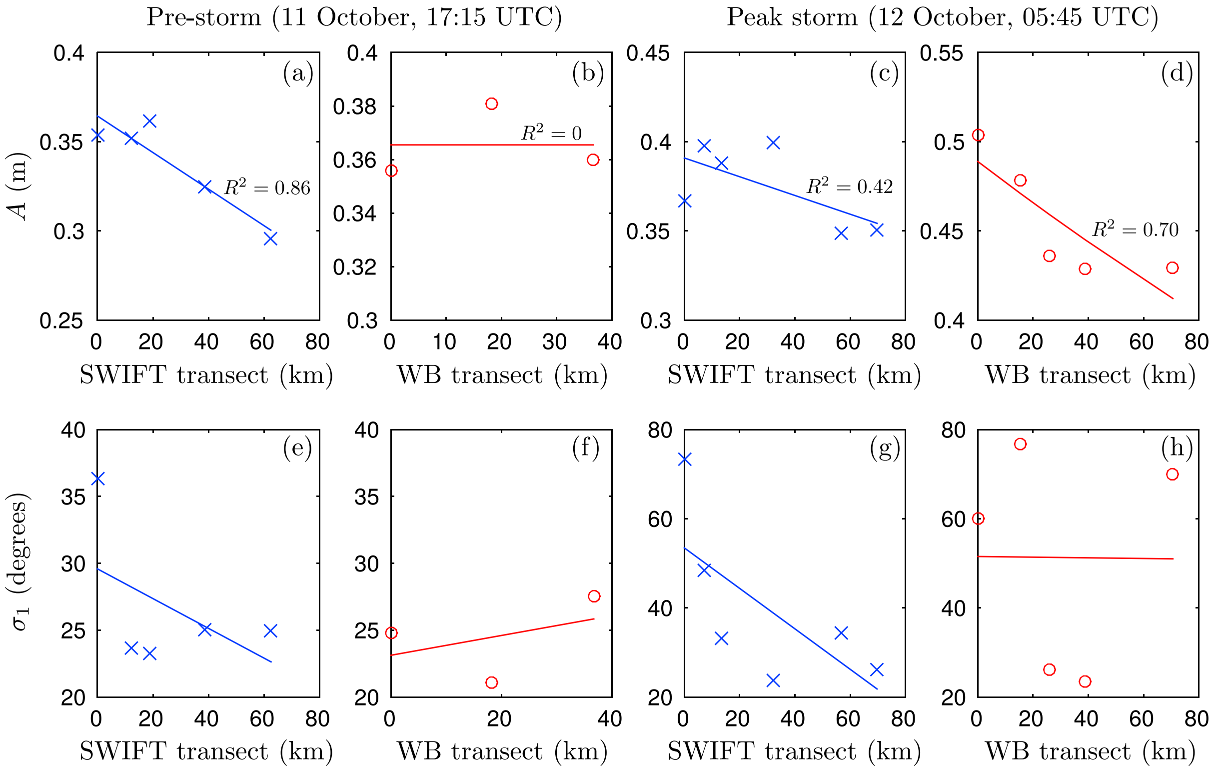

Figure 6. (a)–(d) Spectral amplitude and (e)–(h) directional spread profiles along SWIFT and WB buoy transects at the prestorm (panels a, b, e, and f) and peak storm (panels c, d, g, and h) time intervals. SWIFT data are shown in blue (panels a, c, e, and g), and WB data are shown in red (panels a, c, e, and g). The curves fitted to spectral amplitude and directional spread profiles are shown as solid lines, and the coefficient of determination of the fitting procedure for spectral amplitude decay profiles is shown for reference.

of the WB directional data likely due most likely to the effects of icing, we focus our analysis of directional spreading on the SWIFT data only.

5. Frequency-Averaged Profiles

Following the analysis conducted by Kohout et al. (2014), we first discuss the attenuation experienced by the significant wave height. To do this we fit the decay curve described by (10) to the significant wave height (H_s) data at each time interval t along a transect determined from frequency-averaged directional data metrics. More specifically, the direction of the transect is given by (6) and (7), where θ_1 and σ_1 are replaced by θ_0 and σ_0, respectively. We denote the parameters of the significant wave height decay model by H_0, α_0, and n_0. Analogously, we fit the linear spreading curve (11) to the frequency-averaged directional spread data σ_0 along each transect and denote the rate of directional spreading by parameter β_0 (for the SWIFT buoys only).

The four estimated curve fitting parameters H_0, α_0, n_0, and β_0 at each time t are shown in Figure 7. Parameters obtained from SWIFT and WB data are shown as blue circles and red stars, respectively. The time evolution of H_0 (see panel a), which estimates the significant wave height at the southernmost buoy of each profile, is qualitatively similar to the time series of H_s for both buoy types shown in Figure 1b. This parameter therefore provides a measure of wave energy density for each decay profile, that is, at each time interval. The parameter α_0 mostly fluctuates in the range of values 10^{-6}–10^{-5} over the duration of the wave event (see panel b). Some larger values are observed for both buoy types early in the experiment, that is, up 23:45 UTC on 11 October, which could be a consequence of a more consistent sea ice cover being present before the ice retreat occurs overnight between 11 and 12 October, as discussed in section 2. Larger values can also be seen for WB buoy data only on 12 October between 07:15 and 12:45 UTC. We further note that in 4 of the 106 time intervals with SWIFT attenuation data and 3 of the 53 time intervals with WB attenuation data, we have much smaller values of α_0 (i.e., $< 10^{-9}$), which correspond to wave growth profiles. The third parameter n_0 of the decay model takes its values either close to 0 or 1 (see panel c) for both buoy types, corresponding to near-linear and near-exponential decays, respectively. This clustering of n_0 estimates to the extreme cases

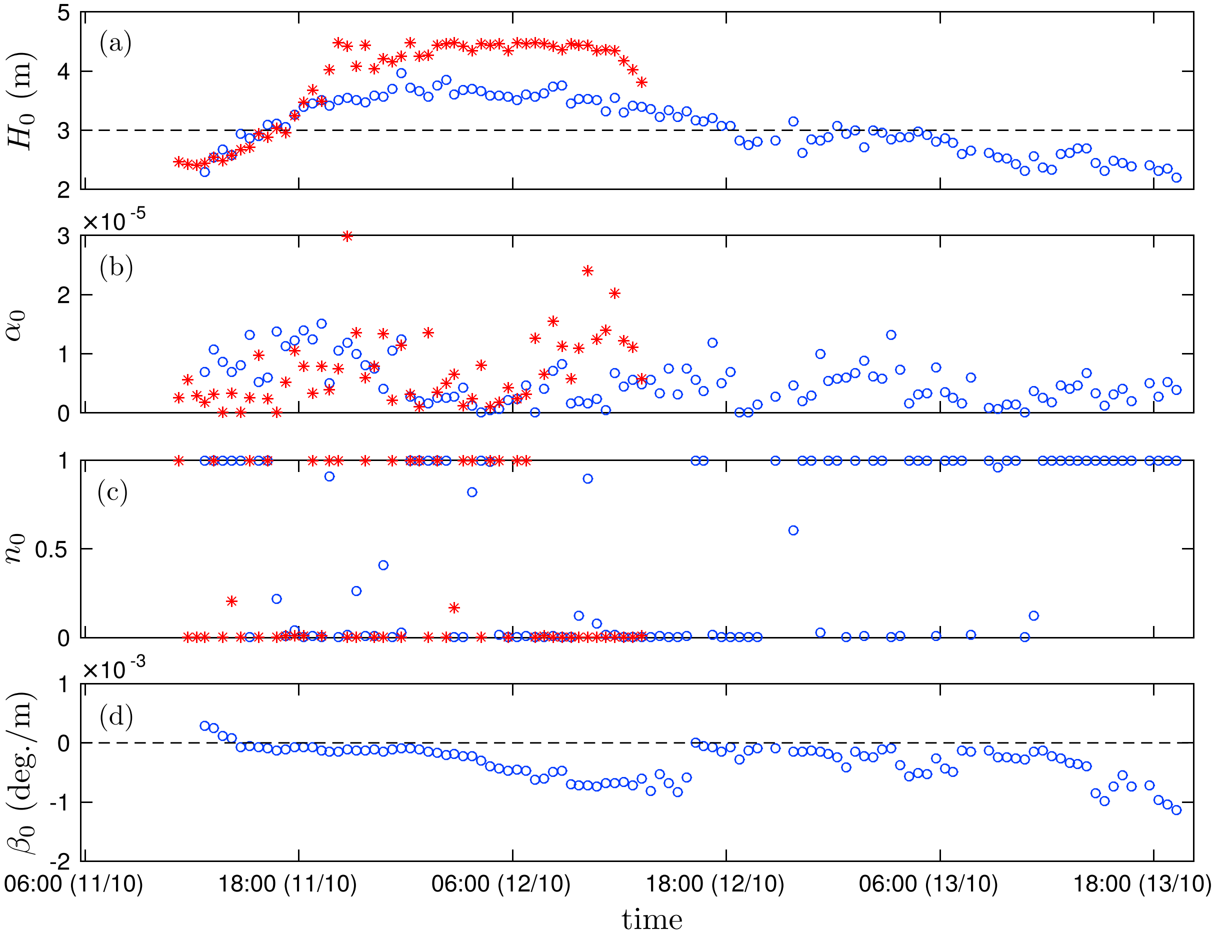

Figure 7. Time series of the curve fitting parameters (a) H_0, (b) α_0, (c) n_0, and (d) β_0 estimated from the significant wave height decay model and the frequency-averaged directional spread linear model, for all SWIFT and WB buoy transects (blue circles and red stars, respectively) containing at least three buoys.

is a consequence of the bounds we imposed on the admissible values for this parameter, and it is likely that we would obtain parameter values outside the bounds by removing these restrictions. The clustering can therefore only be interpreted as the tendency of the wave decay profiles to be either linear or exponential. The time series of the rate of frequency-averaged directional spreading obtained from the SWIFT buoys (see panel d) shows that the parameter β_0 is negative except in the first four time intervals, so that the directional spectrum mainly experiences a narrowing of its directional spread as it advances through the pancake ice cover, likely confirming that dissipative processes dominate over scattering during the wave event.

We further seek to quantify the relationship between significant wave height and the type of wave decay along the transects. To do this we sort the fit parameter $H_0(t)$ in ascending order and cluster them into bins containing 10 and 5 values for the SWIFT and WB data, respectively. In Figures 8a and 8d, the mean H_0 value of each bin is plotted against the median value of the corresponding n_0 parameter estimates in each bin for the two buoy types. We observe the emergence of two regimes from the SWIFT data, that is, $n_0 \approx 1$ for $H_0 \lesssim 3$ m and $n_0 \approx 0$ for $H_0 \gtrsim 3$ m, suggesting exponential decay is more likely for small values of the significant wave height (i.e., calm wave conditions) and linear decay prevails for large values (i.e., storm wave conditions). The abrupt transition between the two regimes is a consequence of looking at the median of n_0 in each H_0 bin. The opposite behavior seems to emerge from the WB data, however, as linear decay dominates at low H_0 values, while exponential decay is more significant at high H_0 values.

We further explore the relationship between type of decay and significant wave height by computing the proportion of approximately linearly decaying profiles, defined such that $n_0 < 0.1$, in each H_0 bin. Figure 8b shows that this quantity increases approximately linearly with H_0 for the SWIFT data, suggesting that the probability significant wave height decays linearly, as opposed to exponentially, increases with wave energy.

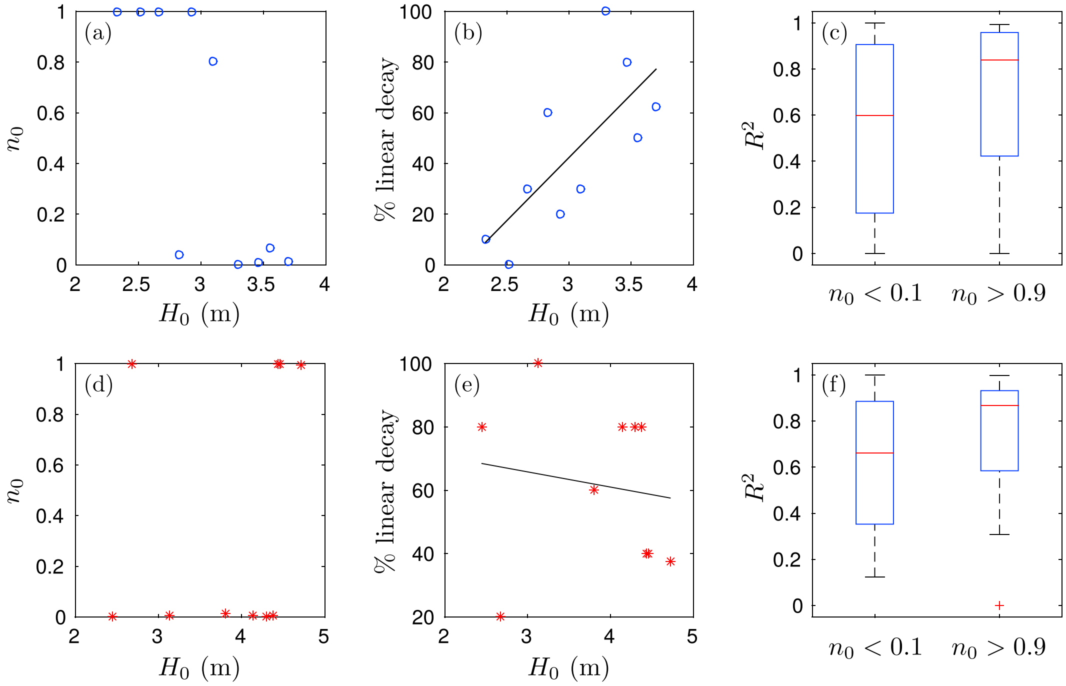

Figure 8. (a, d) Median of n_0 estimates and (b, e) percentage of near-linear decay profiles (i.e., such that $n_0 < 0.1$) plotted against the mean values of 10 H_0 bins, each containing 10 estimates of the parameter. (c, f) Box and whiskers plots of the coefficient of determination R^2 for near-linear decay profiles and near-exponential decay profiles (i.e., such that $n_0 > 0.9$). SWIFT data are shown in panels a–c and WB data in panels d–f.

On the other hand, Figure 8e suggests a weak negative correlation or the lack thereof between the type of attenuation and significant wave height for the WB data, which further indicates significant discrepancy between the two buoy types.

Accordingly, as opposed to the WB data set, the SWIFT observations suggest the piecewise empirical model for the attenuation of significant wave height in pancake ice

$$\frac{\mathrm{d}H_s}{\mathrm{d}s} = \begin{cases} -\alpha_0^{(e)} H_s & \text{if} \quad H_0 \leq 3\,\mathrm{m}, \\ -\alpha_0^{(l)} & \text{if} \quad H_0 > 3\,\mathrm{m}, \end{cases} \tag{12}$$

where $\alpha_0^{(e)} = 4.48 \times 10^{-6} \pm 4.51 \times 10^{-7}\,\mathrm{m}^{-1}$, $\alpha_0^{(l)} = 5.74 \times 10^{-6} \pm 5.42 \times 10^{-7}$, and H_0 can be interpreted as the significant wave height measured closest to the ice edge. The values and error bounds of $\alpha_0^{(e)}$ and $\alpha_0^{(l)}$ are estimated from the samples of fit parameters α. This empirical relationship for significant wave height decay is similar to that found by Kohout et al. (2014) in the Antarctic MIZ. Remarkably, the onset of linear decay at $H_0 = 3$ m obtained here matches that found by those authors, even though they only considered wave observations farther than 100 km from the ice edge and for a different type of ice cover (pancake ice versus ice floes), and the method used to extract the type of decay differs fundamentally from ours. This apparently positive result needs to be counterbalanced by the fact that no correlation between decay type and significant wave height was found from the WB data analysis. In addition, it is important to note that the validity of the regime shift between near-linear and near-exponential decays identified with the dimensional value of $H_s = 3$ m is limited to the frequency range covered by the spectra analyzed here, that is, $f \approx 0.05$–0.5 Hz and to the ice type and thickness encountered during the wave event analyzed here. Although we do not claim that $H_s = 3$ m is a universal threshold for the observed linear versus exponential decay regime shift, the fact that we find a concordant value with that of Kohout et al. (2014) is worth highlighting and requires further investigation beyond the scope of the present study. We further note that Stopa et al. (2018), who analyzed the same wave event with synthetic aperture radar data but deeper in the ice-covered ocean, found evidence of regime shifts in wave decay rates as a function of distance from the ice edge likely due to changing ice conditions. The evolving ice morphology, which is probably correlated to wave energy density, may therefore also partly explain our observed regime change.

In Figures 8c and 8f, we show a box and whiskers plot of the coefficient of determination estimates R^2 corresponding to near-linear decay profiles, that is, $n_0 < 0.1$, and near-exponential decay profiles, that is, $n_0 > 0.9$. We observe that the median of R^2 for near-exponential decay profiles (≈ 0.85) is much larger than that for near-linear decay profiles (≈ 0.6) for both wave buoys. The variability of R^2 is also much larger for $n_0 < 0.1$ than for $n_0 > 0.9$, so that exponential decay profiles are generally better fits to the data than linear decay profiles. As a consequence, the linear decay estimates found by our model may be a way for the curve fitting procedure to adjust to more scattered data during a large wave event.

6. Frequency-Resolving Profiles

We now analyze the decay profile of the spectral amplitude $A(t, f)$. At each time interval t and frequency f, the parameters A_0, α, and n of the wave decay model (10) are estimated using the curve fitting procedure described in section 4. We generated 3,033 (A_0, α, and n) parameter triplets from the SWIFT data and 1,790 from the WB data. We depict the estimated parameter values as time-frequency spectrograms in Figures 9 and 10 (see panels a–c) associated with the SWIFT and WB data, respectively. This allows us to visualize the frequency dependence of each parameter at a time interval t by looking at a vertical slice of the surface plot. White areas in the spectrograms correspond to profiles discarded from the curve fitting analysis either due to the number of active buoys being two or less or because the parameters estimated by the fitting procedure were complex.

The spectrograms associated with the parameter A_0 (see panel a in Figures 9 and 10) describes the time evolution of the spectral amplitude through the wave event. We can observe the peak of the spectrum at a frequency slightly above 0.1 Hz growing in energy until about 06:00 UTC on 12 October at the peak of the wave event and then decreasing gradually as the storm dies out. The effect of the storm on spectral amplitude at higher frequencies is not noticeable. In contrast, the parameter α is much more sensitive to frequency than the time evolution of the storm event (see panel b in Figures 9 and 10), with values increasing by up to an order of magnitude from low to high frequencies for the SWIFT data. The spectrograms of the parameter n clearly shows a predominance of near-exponential decay profile, that is, $n \approx 1$. A few patches of n values close to 0, corresponding to near-linear decay profiles, are observed, but it is not clear what these are associated with. In particular, for the WB data, near-linear decay is observed after 07:00 UTC on 12 October for all frequencies $f > 0.1$ Hz, which is consistent with the analysis of the frequency-averaged profiles (see Figure 7c). To understand better the emergence of the linear decaying profiles, we now conduct a correlation analysis of the parameter n with respect to both frequency and spectral amplitude.

Figures 11a–11c investigate the dependence of the parameter n on wave frequency for both the SWIFT data (blue circles) and WB data (red stars). Specifically, for each frequency component, the median of the parameter n is shown in panel a, the percentage of linearly decaying profiles, that is, such that $n < 0.1$, in panel b and the median of the coefficient of determination R^2 in panel c. As suggested by the SWIFT data spectrogram in Figure 9c, the spectral amplitude decay profiles show a tendency to be exponentially decaying for all frequencies as the median value of n at each frequency is larger than 0.8 for $f < 0.4$ Hz and larger than 0.6 for all frequencies. The percentage of linearly decaying profiles remains smaller than 10% except around the peak frequency of the spectrum, suggesting some effect of wave amplitude on the type of decay profile. Now looking at panel c, the median value of R^2 is consistently above 0.5, except in the low frequency range $f < 0.1$ Hz, for which SWIFT buoys have known limitations (discussed earlier) to resolve spectral densities accurately. Although exponential decay is also mainly observed for the WB data with the median $n > 0.5$ for all frequencies, the percentage of linearly decaying profiles (see panel b) does not seem to depend on the shape of the spectrum with values of 20–40% over most of the frequency range (~0.1–0.4 Hz). The percentage of linearly decaying profile reaches its maximum for $0.3 < f < 0.4$ Hz, for which $n \approx 0$ in the early and late stages of the wave event (see spectrogram in Figure 10c). As opposed to the SWIFT data, the type of decay seems to depend more on time than frequency or energy density for the WB data.

Figures 11d–11f show the spectral amplitude dependence of the same n-related metrics as in panels a–c. More specifically, the estimated parameter values A_0 are sorted in ascending order and clustered into bins containing 50 values for both buoy types. The median of n, the percentage of linearly decaying profiles and the median of R^2 are then plotted in panels d–f, respectively, against the mean of the A_0 bins. For the SWIFT data, we observe that the median of n in each A_0 bin is consistently larger than 0.8 except at the single bin with mean value $A_0 \approx 0.4$ m. This confirms the prevalence of exponentially decaying spectral amplitude profiles

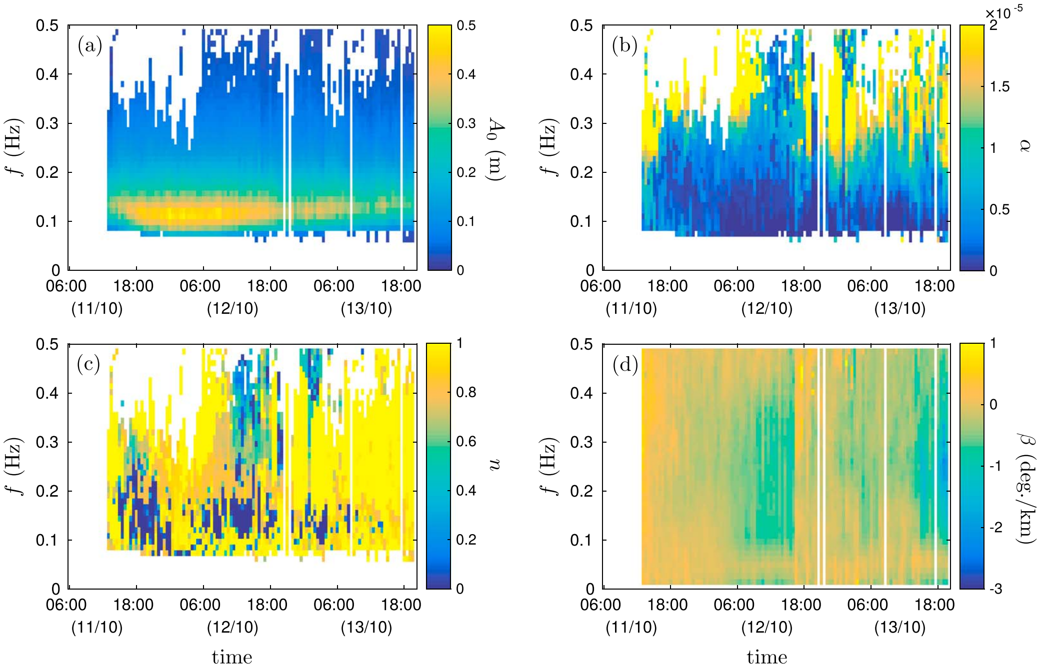

Figure 9. Time-frequency spectrograms of the estimated parameters of the spectral amplitude decay model (10), that is, (a) $A_0(t,f)$, (b) $\alpha(t,f)$, and (c) $n(t,f)$ and the linear rate of directional spread (d) $\beta(t,f)$, for SWIFT transects of at least three buoys.

for this data set. Interestingly, a positive linear trend can be seen between the percentage of linearly decaying profiles and spectral wave amplitude, similar to that found for the frequency-averaged profiles. Although this percentage always remains below 50%, so that the median value of n stays close to 1, extrapolating the trend would suggest that linear decay would become more prevalent for more energetic waves than those observed during the wave event analyzed here. It should be noted, however, that the coefficient of determination decreases to $R^2 < 0.5$ for spectral wave amplitudes $A_0 > 0.35$ m, so the fitting procedure does not perform as well as for lower spectral amplitude profiles. The dependence of n on spectral amplitude for the WB data does not show the same trends, as the percentage of linearly decaying profiles fluctuates about 25–30% for all values of A_0.

As discussed earlier, it is not clear what physical processes would be responsible for the linear, as opposed to exponential, wave decay exhibited by the SWIFT data. We observe, however, that cases of linear decay are associated with very small values of the parameter α, which can be interpreted as an attenuation coefficient. We therefore envisage two possible explanations for linearly decaying profiles: (i) The ice cover has almost no

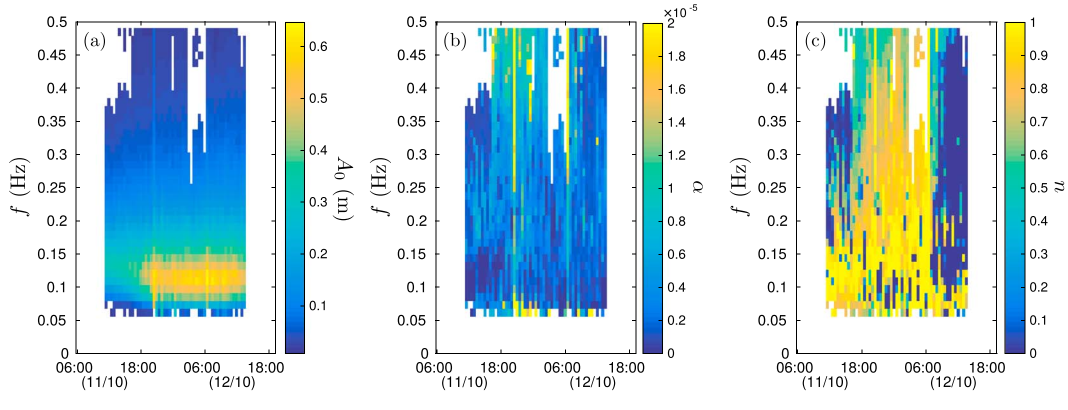

Figure 10. Time-frequency spectrograms of the estimated parameters of the spectral amplitude decay model (10), that is, (a) $A_0(t,f)$, (b) $\alpha(t,f)$, and (c) $n(t,f)$, for WB transects of at least three buoys.

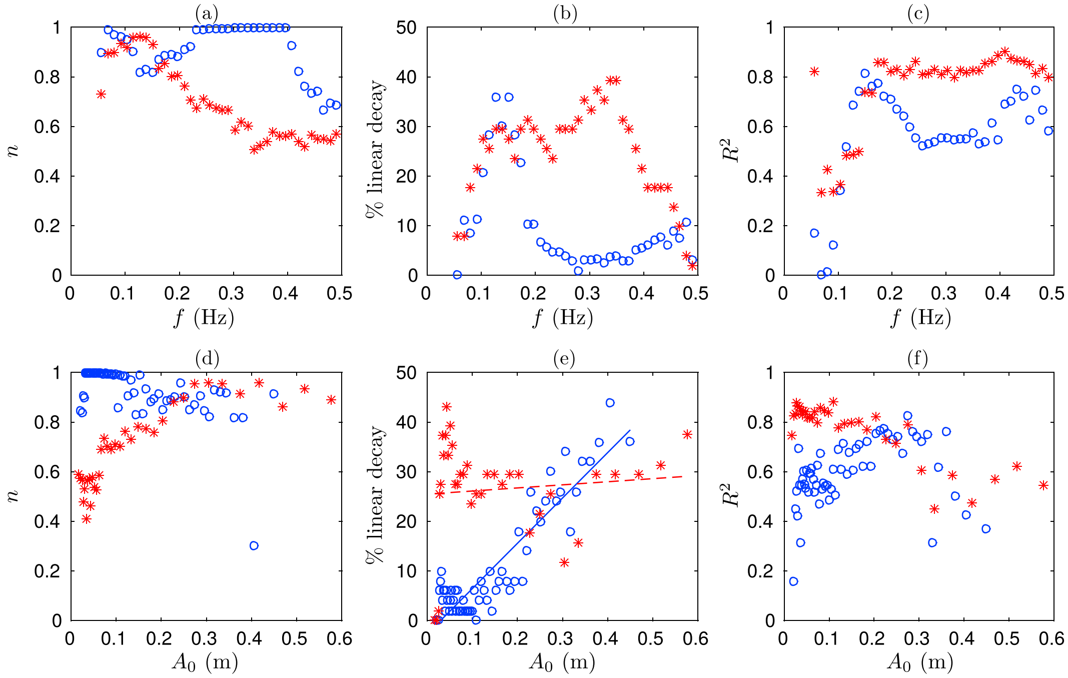

Figure 11. (a, d) Median value of the parameter n, (b, e) percentage of linearly decaying profiles, and (c, f) median of the coefficient of determination R^2 are plotted against (a–c) wave frequency and (d–f) the mean of 60 A_0 bins. SWIFT and WB data are shown as blue circles and red stars, respectively.

effect on wave evolution so that the small observed decay is a consequence of mechanisms inherent to wave propagation as in open water, or (ii) the fitted decay curve has little sensitivity to n for small values of α, for which the linearization of the exponential decay is almost identical to the exponential curve itself, so that the fitting procedure randomly selects $n \approx 0$ or 1 with no apparent effect on the goodness of fit.

We now turn our attention to the rate of directional spreading parameter $\beta(t, f)$, which is estimated for each SWIFT directional spread profile by fitting the straight line (11). We obtain 4,452 estimates of the parameter, which we depict in the time-frequency spectrogram in Figure 9d. We observe that most β values are close to 0. Closer inspection reveals that most of these values are actually negative. Some time periods and frequency ranges are associated with stronger negative β values, for example, from 06:00 to 16:00 on 12 October and for $f = 0.1$–0.4 Hz, but it is not clear what causes this more intense narrowing of the directional spectrum. One possibility is that the southernmost buoys in the associated directional spread profiles are located in a low concentration zone or in open water, so that an abrupt decrease in directional spread occurs at the ice edge. Such a change in directional spread was observed in the special cases investigated in Figure 6 (see panels e and g), in which the directional spread seems to be slightly increasing after an initial abrupt decrease, which could suggest that scattering may become important deep into the ice-covered ocean in a certain frequency range. We note that waves traveling in directions not collinear with the transect could also explain the observed variability in the directional spread data and the apparent small spreading discussed here. Closer inspection of the data set shows that a change from large negative spreading to small positive spreading occurs between the time intervals centered at 15:45 and 16:15 UTC on 12 October, and for frequencies $f \approx 0.1$–0.2 Hz. The reason for this change is that the two southernmost buoys at 15:45 were removed from the profile at 16:15, so that the abrupt decrease in σ_1 observed near the ice edge is not captured by the second profile.

We further investigate how β depends on wave frequency and spectral amplitude in Figure 12. For each frequency component, the mean of β is plotted in panel a and the standard deviation is plotted in panel b. Note that a sample of 106 β estimates is used for each frequency. As discussed earlier, all β values are negative. The rate of directional narrowing, that is, $-\beta$, is larger in the frequency range 0.1–0.4 Hz, peaking at $f \approx 0.25$ Hz, while it is smaller at low and high frequencies. The variability of this rate is also larger in this midfrequency range, suggesting that the effect of the sea ice on the evolution of the wave spectrum is most pronounced

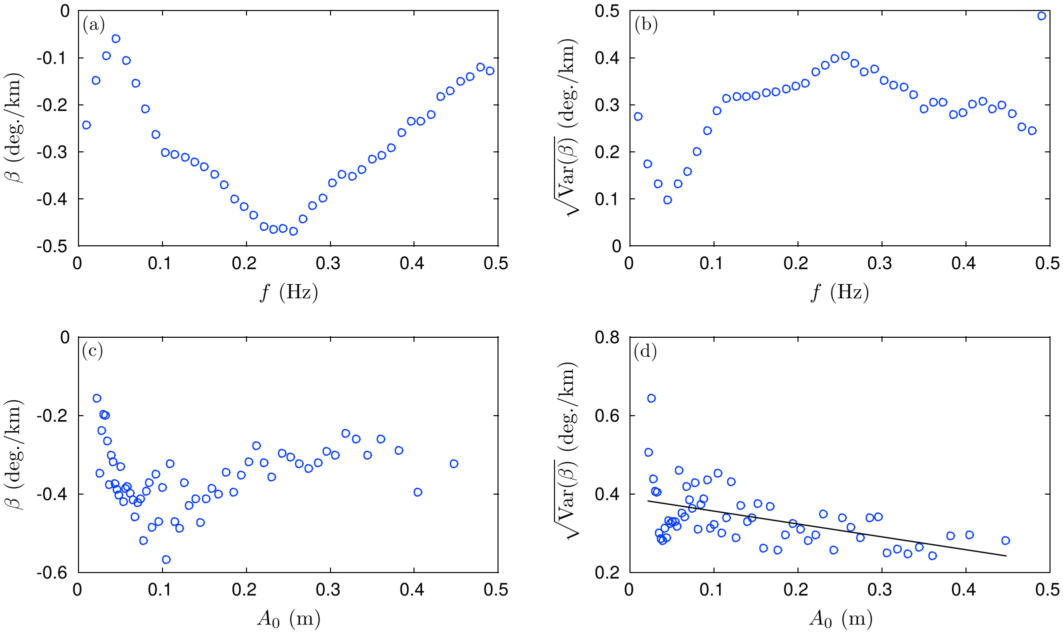

Figure 12. (a, c) Mean value and (b, d) standard deviation of the SWIFT rate of directional spreading β plotted against (a, b) wave frequency and (c, d) the mean of 60 A_0 bins.

in this frequency range. The changing ice conditions observed during the wave event and the changing number of buoys present in each profile are likely responsible for this variability.

We use the same A_0 binning as in Figures 11d–11f to analyze the dependence of β on spectral amplitude. Figures 12c and 12d show the mean value and standard deviation of β, respectively, against the mean of each A_0 bin. We observe that β exhibits little dependence on the spectra amplitude while the variability in the rate of directional spreading clearly decreases with this quantity. This suggests that larger waves are less affected by the changing ice conditions and therefore processes governing wave/ice interactions, which is consistent with our observations for the decay of large amplitude waves.

7. Exponential Decay Model

The analysis conducted in section 6 suggests that most spectral amplitude profiles are best fitted with an exponential decay curve. Therefore, we now reprocess each spectral amplitude profile generated with at least three SWIFT buoys by fitting through them the exponential decay curve

$$A(s) = A_0^e \, \mathrm{e}^{-\alpha^e s}, \tag{13}$$

where A_0^e and α^e are the parameters we seek to estimate. The latter parameter, which we refer to as the attenuation coefficient, is of particular interest, as we seek to describe its relationship to wave frequency as was done by Meylan et al. (2014) in the Antarctic MIZ. The same nonlinear least square fitting procedure described in section 4 is used here. We obtain 4,028 estimates of the two decay model parameters for the SWIFT data and 2,014 estimates for the WB data, that is, more than with the decay model (10), due to the fact that we do not need to impose bounds on the parameters, so that the fitting routine always returns positive real values of the parameters.

Time-frequency spectrograms for $A_0^e(t,f)$ and $\alpha^e(t,f)$ are shown in Figures 13a and 13b, respectively, for the SWIFT data and Figures 13c and 13d, respectively, for the WB data. The spectrograms look very similar to those of A_0 and α in Figures 9 and 10 (see panels a and b), which is expected given that the majority of decay profiles were found to be near exponential. The attenuation coefficient reaches values close to or even above 10^{-4} m^{-1} at high frequencies, which is larger than the maximum of α obtained in section 6, noting that we could not obtain many estimates of α at high frequencies due to the fitting algorithm returning complex values.

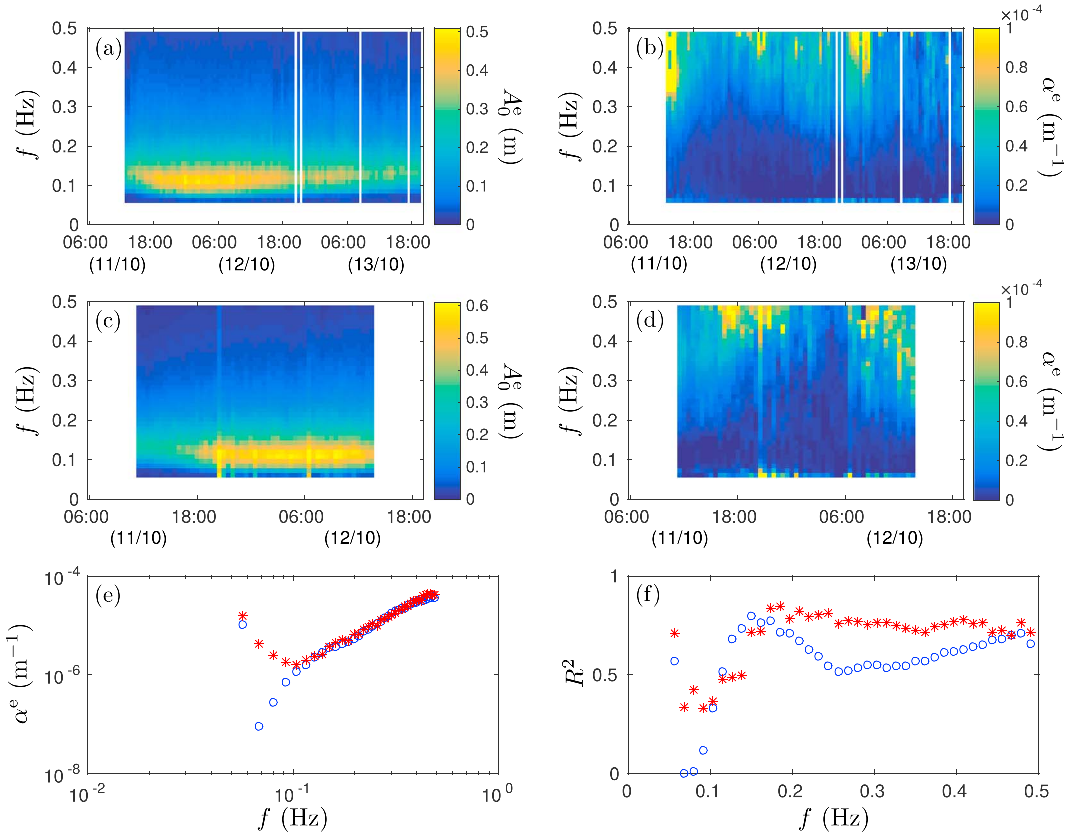

Figure 13. Time-frequency spectrograms of the estimated parameters of the spectral amplitude exponential decay model (13), that is, (a, c) $A_0^e(t,f)$ and (b, d) $\alpha^e(t,f)$, for SWIFT (panels a and b) and WB (panels c and d) transects of at least three buoys. (e) Median value of the attenuation coefficient α^e and (f) median of the coefficient of determination R^2 are plotted against wave frequency, for SWIFT and WB data (blue circles and red stars, respectively).

Figure 13e shows the median value of α^e for each frequency component on a log-log plot for both buoy types. The corresponding median R^2 values are depicted in panel f. The goodness of fit is found to be very poor for low frequencies (i.e., $R^2 < 0.5$), so we do not consider this regime in order to find an empirical relationship between α^e and f. Previous studies by Meylan et al. (2014) and Wadhams (1975) suggest that a power law exists between these two quantities. We therefore performed a fit of the form

$$\alpha^e(f) = af^b, \quad \text{for} \quad 0.1\,\text{Hz} < f < 0.5\,\text{Hz}, \tag{14}$$

for both data sets and found the values $a \approx 2.31\times10^{-4}$ and $b \approx 2.26$ from the SWIFT data and $a \approx 2.37\times10^{-4}$ and $b \approx 2.22$ from the WB data, which is remarkably consistent given the discrepancies between the two data sets discussed throughout the paper. These values of b are also consistent with those found in past studies, noting that the frequency range considered here extends to much higher frequencies than those reported by Meylan et al. (2014) and Wadhams (1975). It should be noted that our b estimates are substantially different from that of Meylan et al. (2018), that is, $b \approx 3.6$, obtained for the same data set extended to a longer time period of measurements than that considered here, based on the analysis conducted by Cheng et al. (2017). We argue that the discrepancy is too large to be explained by the extended period of measurements but reflects the method used to extract attenuation coefficients instead. While we used attenuation profiles with three or more buoys to extract the attenuation rates, Cheng et al. (2017) only looked at pairs of buoys, as discussed earlier, leading them to discard many buoy pairs showing local wave growth with the consequent effect of overestimating attenuation.

8. Conclusions

We described an analysis of directional wave data collected in the ice-covered Beaufort Sea by an array of 11 wave sensors (six SWIFT and five WB wave buoys) during a 3-day large wave event in October 2015. Pancake ice dominated during this event in the location of the experiment. We found significant differences between the directional spectra measured by the two buoy types, possibly caused by the observed icing experienced by the two sensors, so that wave data were analyzed separately for the SWIFT and WB buoys. A method has been proposed to analyze (i) wave decay and (ii) changes in wave directionality as the wave spectrum propagates in the pancake ice cover. Two well-established wave amplitude/height metrics derived from wave energy spectral density were considered to quantify wave decay, that is, the significant wave height, which is frequency averaged, and the spectral amplitude, which is frequency resolving. Analogously, we defined frequency-averaged and frequency-resolving versions of the directional spread. A wave transect, defined in terms of the wave directionality data of three or more buoys, was obtained for each buoy type, time interval, and frequency. We then fitted a nonlinear decay curve with three parameters through the wave amplitude/height data along each transect. The decay model was chosen so that it captures both linear and exponential decays for extreme values of a parameter. These two decay types were observed for the same data set collected in the Antarctic MIZ by analyzing the two metrics considered here. We further estimated the change in wave directionality along each transect by fitting a linear curve through the corresponding directional spread profiles. Only SWIFT wave directionality data were analyzed because icing on the WB buoys caused directional information to be unreliable.

Key findings of the wave decay curve fitting analysis were the following:

1. The vast majority of parameter estimates are associated with either near-linear or near-exponential decays for both buoys types.
2. For SWIFT data, the probability of linear wave decay, as opposed to exponential, is positively correlated with energy density, for both the significant wave height and the spectral amplitude metrics, although there is evidence that goodness of fit decreases in concert. No corresponding correlation was observed between linear decay and energy density or frequency for the WB data, however.
3. The decay of significant wave height measured from the SWIFT buoys shifts from predominantly exponential to predominantly linear when reaching the value of approximately 3 m, which is remarkably consistent with what was found by Kohout et al. (2014) for the Antarctic data set. The WB data do not exhibit this regime change, however.
4. The decay of spectral amplitudes remains predominantly exponential for the range of spectral amplitude estimated values observed during the wave event analyzed here.

We also conducted a supplemental exponential curve fitting procedure on the spectral amplitude decay profiles and obtained a power law relationship between the attenuation coefficient α^e and wave frequency f of the form $\alpha^e \propto f^{2.2}$ for both data sets, a value which is consistent with past studies. We recommend that our empirical power law is included as a parameterization options for wave decay by pancake ice as part of a future version of WW3 to complement that available for an ice floe-dominated MIZ from the Antarctic data set (Meylan et al., 2014).

The onset of linear decay for large waves observed for the SWIFT data raises two key issues: (i) It remains unclear what physical mechanism can cause a decay that is not asymptotically approaching 0, and (ii) the dimensional value of $H_s = 3$ m found as the threshold for the linear decay regime can only be considered as valid for the restricted range of wave and ice conditions encountered in the wave event analyzed here. Resolution of (i) with theory is crucial before formally adopting the linear decay law as a feature of the wave/pancake ice system. Alternatively, there is a chance that such a behavior is an artifact of the method used to analyze wave attenuation, as may be suggested by the WB data and the fact that our linear decay profiles are associated with poorer fits.

Key findings of the directional spreading analysis were the following:

1. Both frequency-averaged and frequency-resolved metrics of the directional spread exhibit a decrease with distance of propagation in the pancake ice cover, confirming well-established knowledge that dissipative processes dominate over scattering in governing the ice effects on wave evolution for this type of ice cover.
2. Directional narrowing frequency dependence is more pronounced in the range 0.1 – 0.4 Hz, reaching its peak at approximately 0.25 Hz, while it is nearly insensitive to wave energy.

Currently, directional spreading is only parametrized in WW3 as an isotropic directional redistribution function of wave components from scattering. It can also result from wind forcing and angular dispersion due to wave refraction at the ice edge. The directional data obtained here show that directional narrowing further needs to be included to model the evolution of the directional spectrum in a pancake ice field. Further investigations into the relationship between wave dissipation, directional spreading, and ice conditions are needed to implement a process-informed parameterization of directional redistribution in WW3.

Acknowledgments
The data analyzed in this study can be accessed from http://www.apl.washington.edu/arcticseastate, under the Data tab. The authors are grateful to all the project team members who contributed to the design of the wave buoys, the collection of the data during the Sea State voyage, and the initial processing of the data. The Matlab codes and data files created for the analysis reported here can be accessed through https://www.maths.otago.ac.nz/fmontiel/Data. The authors would like to thank Sunkun Cheng and Hayley Shen for their assistance at the initial stage of the data set analysis, as well as the rest of the Sea State DRI team for constructive discussions that have improved the paper. The authors acknowledge funding from Office of Naval Research, awards N00014-131-0279 (Montiel and Squire), N00014-131-0284 (Thomson), and N00014-131-0290 (Doble and Wadhams). First author Montiel further acknowledges support from the New Zealand Ministry of Business, Innovation and Employment through the Deep South National Science Challenge (contract C01X1445). V. A. S. also thanks the Isaac Newton Institute for Mathematical Sciences for support and hospitality during the program *The Mathematics of Sea Ice Phenomena* when some of the research reported in this paper was undertaken, supported by EPSRC grant EP/K032208/1.

References

Aksenov, Y., Popova, E. E., Yool, A., Nurser, A. J. G., Williams, T. D., Bertino, L., & Bergh, J. (2017). On the future navigability of Arctic sea routes: High-resolution projections of the Arctic Ocean and sea ice. *Marine Policy*, *75*, 300–317.

Cheng, S., Rogers, W. E., Thomson, J., Smith, M., Doble, M., Wadhams, P., et al. (2017). Calibrating a viscoelastic sea ice model for wave propagation in the Arctic fall marginal ice zone. *Journal of Geophysical Research: Oceans*, *122*, 8770–8793. https://doi.org/10.1002/2017JC013275

Comiso, J. C. (2012). Large decadal decline of the Arctic multiyear ice cover. *Journal of Climate*, *25*, 1176–1193.

Doble, M. J., De Carolis, G., Meylan, M. H., Bidlot, J.-R., & Wadhams, P. (2015). Relating wave attenuation to pancake ice thickness, using field measurements and model results. *Geophysical Research Letters*, *42*, 4473–4481. https://doi.org/10.1002/2015GL063628

Kohout, A. L., Penrose, B., Penrose, S., & Williams, M. J. M. (2015). A device for measuring wave-induced motion of ice floes in the Antarctic marginal ice zone. *Annals of Glaciology*, *56*(69), 415–424.

Kohout, A. L., Williams, M. J. M., Dean, S. M., & Meylan, M. H. (2014). Storm-induced sea-ice breakup and the implications for ice extent. *Nature*, *509*, 604–607.

Kuik, A. J., van Vledder, G. Ph., & Holthuijsen, L. H. (1988). A method for the routine analysis of pitch-and-roll buoy wave data. *Journal of Physical Oceanography*, *18*, 1020–1034.

Melia, N., Haines, K., & Hawkins, E. (2016). Sea ice decline and 21st century trans-Arctic shipping routes. *Geophysical Research Letters*, *43*, 9720–9728. https://doi.org/10.1002/2016GL069315

Meylan, M. H., Bennetts, L. G., & Kohout, A. L. (2014). In situ measurements and analysis of ocean waves in the Antarctic marginal ice zone. *Geophysical Research Letters*, *41*, 5046–5051. https://doi.org/10.1002/2014GL060809

Meylan, M. H., Bennetts, L. G., Mosig, J. E. M., Rogers, W. E., Doble, M. J., & Peter, M. A. (2018). Dispersion relations, power laws, and energy loss for waves in the marginal ice zone. *Journal of Geophysical Research: Oceans*, *123*, 3322–3335. https://doi.org/10.1002/2018JC013776

Montiel, F., & Squire, V. A. (2017). Modelling wave-induced sea ice break-up in the marginal ice zone. *Proceedings of the Royal Society A*, *473*(20170258).

Montiel, F., Squire, V. A., & Bennetts, L. G. (2016). Attenuation and directional spreading of ocean wave spectra by large random arrays of ice floes. *Journal of Fluid Mechanics*, *790*, 492–522.

Mosig, J. E. M., Montiel, F., & Squire, V. A. (2015). Comparison of viscoelastic-type models for ocean wave attenuation in ice-covered seas. *Journal of Geophysical Research: Oceans*, *120*, 6072–6090. https://doi.org/10.1002/%202015JC010881

Rogers, W. E., Thomson, J., Shen, H. H., Doble, M. J., Wadhams, P., & Cheng, S. (2016). Dissipation of wind waves by pancake and frazil ice in the autumn Beaufort Sea. *Journal of Geophysical Research: Oceans*, *121*, 7991–8007. https://doi.org/10.1002/2016JC012251

Shen, H. H., & Squire, V. A. (1998). Wave damping in compact pancake ice fields due to interactions between ice cakes. In M. Jeffries (Ed.), *Antarctic Science Research Series* (vol. 74, pp. 325–341). Washington D.C: American Geophysical Union.

Squire, V. A., & Montiel, F. (2016). Evolution of directional wave spectra in the marginal ice zone: A new model tested with legacy data. *Journal of Physical Oceanography*, *46*, 3121–3137.

Stammerjohn, S., Massom, R., Rind, D., & Martinson, D. (2012). Regions of rapid sea ice change: An inter-hemispheric seasonal comparison. *Geophysical Research Letters*, *39*, L06501. https://doi.org/10.1029/2012GL050874

Stopa, J. E., Ardhuin, F., Thomson, J., Smith, M. M., Kohout, A. L., Doble, M., & Wadhams, P. (2018). Wave attenuation through an Arctic marginal ice zone on 12 October 2015: 1. Measurement of wave spectra and ice features from Sentinel 1A. *Journal of Geophysical Research: Oceans*, *123*, 3619–3634. https://doi.org/10.1029/2018JC013791

Strong, C., & Rigor, I. G. (2013). Arctic marginal ice zone trending wider in summer and narrower in winter. *Geophysical Research Letters*, *40*, 4864–4868. https://doi.org/10.1002/grl.50928

Sutherland, P., Brozena, J., Rogers, W. E., Doble, M., & Wadhams, P. (2018). Airborne remote sensing of wave propagation in the marginal ice zone. *Journal of Geophysical Research: Oceans*, *123*, 4132–4152. https://doi.org/10.1029/2018JC013785

Sutherland, P., & Gascard, J.-C. (2016). Airborne remote sensing of ocean wave directional wavenumber spectra in the marginal ice zone. *Geophysical Research Letters*, *43*, 5151–5159. https://doi.org/10.1002/2016GL067713

The WAVEWATCH III® Development Group(2016). User manual and system documentation of WAVEWATCH III® version 5.16 (*Tech. Rep. 329*). College Park, MD, USA: NOAA/NWS/NCEP/MMAB.

Thomson, J. (2012). Wave breaking dissipation observed with SWIFT drifters. *Journal of Atmospheric and Oceanic Technology*, *29*, 1866–1882.

Thomson, J. (2015). ONR Sea State DRI cruise report: R/V Sikuliaq, fall 2015 865 (SKQ201512S) (*Technical report*). Seattle, WA: University of Washington.

Thomson, J., Ackley, S., Girard–Ardhuin, F., Ardhuin, F., Babanin, A., Boutin, G., et al. (2018). Overview of the Arctic Sea State and Boundary Layer Physics Program. *Journal of Geophysical Research: Oceans*, *123*. https://doi.org/10.1002/2018JC013766

Thomson, J., Ackley, S., Shen, H. H., & Rogers, W. E. (2017). The balance of ice, waves, and winds in the Arctic autumn. *Eos*, *98*.

Thomson, J., Fan, Y., Stammerjohn, S., Stopa, J., Rogers, W. E., Girard-Ardhuin, F., et al. (2016). Emerging trends in the sea state of the Beaufort and Chukchi Seas. *Ocean Model*, *105*, 1–12.

Thomson, J., & Rogers, W. E. (2014). Swell and sea in the emerging Arctic Ocean. *Geophysical Research Letters*, *41*, 3136–3140. https://doi.org/10.1002/2014GL059983

Wadhams, P. (1975). Airborne laser profiling of swell in an open ice field. *Journal of Geophysical Research*, *80*, 4520–4528.

Wadhams, P., Squire, V. A., Ewing, J. A., & Pascal, R. W. (1986). The effect of the marginal ice zone on the directional wave spectrum of the ocean. *Journal of Physical Oceanography*, *16*, 358–376.

Wadhams, P., Squire, V. A., Goodman, D. J., Cowan, A. M., & Moore, S. C. (1988). The attenuation rates of ocean waves in the marginal ice zone. *Journal of Geophysical Research*, *93*, 6799–6818.